JACS
JOURNAL OF THE AMERICAN CHEMICAL SOCIETY
Article
pubs.acs.org/JACS

Hydrogen Doped Metal Oxide Semiconductors with Exceptional and Tunable Localized Surface Plasmon Resonances

Hefeng Cheng,[†,⊥] Meicheng Wen,[†,⊥] Xiangchao Ma,[§,#] Yasutaka Kuwahara,[†,‡] Kohsuke Mori,[†,‡] Ying Dai,[§] Baibiao Huang,[*,∥] and Hiromi Yamashita[*,†,‡]

[†]Division of Materials and Manufacturing Science, Graduate School of Engineering, Osaka University, 2-1 Yamadaoka, Suita, Osaka 565-0871, Japan

[‡]Unit of Elements Strategy Initiative for Catalysts & Batteries (ESICB), Kyoto University, Katsura, Kyoto 615-8520, Japan

[§]School of Physics, and [∥]State Key Laboratory of Crystal Materials, Shandong University, Jinan 250100, China

Supporting Information

ABSTRACT: Heavily doped semiconductors have recently emerged as a remarkable class of plasmonic alternative to conventional noble metals; however, controlled manipulation of their surface plasmon bands toward short wavelengths, especially in the visible light spectrum, still remains a challenge. Here we demonstrate that hydrogen doped given MoO_3 and WO_3 via a facile H-spillover approach, namely, hydrogen bronzes, exhibit strong localized surface plasmon resonances in the visible light region. Through variation of their stoichiometric compositions, tunable plasmon resonances could be observed in a wide range, which hinge upon the reduction temperatures, metal species, the nature and the size of metal oxide supports in the synthetic H_2 reduction process as well as oxidation treatment in the postsynthetic process. Density functional theory calculations unravel that the intercalation of hydrogen atoms into the given host structures yields appreciable delocalized electrons, enabling their plasmonic properties. The plasmonic hybrids show potentials in heterogeneous catalysis, in which visible light irradiation enhanced catalytic performance toward *p*-nitrophenol reduction relative to dark condition. Our findings provide direct evidence for achieving plasmon resonances in hydrogen doped metal oxide semiconductors, and may allow large-scale applications with low-price and earth-abundant elements.

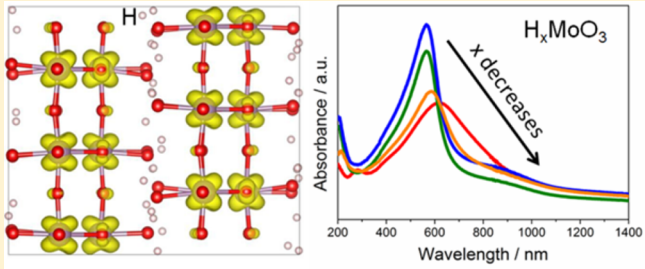

1. INTRODUCTION

The interaction between light and matter is the fundamental principle of many physical processes and underpins a host of disciplines ranging from metamaterials to waveguides and plasmonics.[1,2] With the advent of nanoscience and nanotechnology, recent years have witnessed drastic advances in plasmonic nanostructures, where coherent oscillation of free electrons upon incident light gives rise to the localized surface plasmon resonance (LSPR);[3] this phenomenon is concomitant with optical near-field amplification, and has led to a variety of application domains in, for instance, surface-enhanced Raman scattering (SERS),[4] biological detection,[5] and energy storage and conversion.[6] Noble metals of Au and Ag are among the most studied conventional plasmonic materials that display sharp plasmon modes in the spectrum of visible light region.[7−12] Alternatively, highly doped semiconductors represent another important class of plasmonic materials,[13,14] which mainly involve transparent conducting oxides (TCO)[15−17] and transition metal oxides/chalcogenides.[18−22] In terms of crustal abundance of elements and lower optical losses,[23] highly doped semiconductors may outperform their noble-metal counterparts in serving as building blocks, particularly for metamaterials and transformation optics devices.

To sustain surface plasmons in a semiconductor, the concentration of accumulated free carriers (electrons or holes) must be above the threshold value, turning its real part of dielectric permittivity negative.[2] In general, this prerequisite in semiconductors is met through heavy doping that introduces aliovalent heteroatoms or lattice vacancies.[24] As a consequence, the upper limit of carrier concentration in semiconductors is determined by the equilibrium between doping and compensation, thereby leading to their plasmon resonance frequency predominantly in near- to mid-infrared light regime.[14] As the smallest atoms in nature, hydrogen atoms are able to migrate and exist in a body of interstitial sites of inorganic compounds, while avoiding larger structural expansion. Hydrogen doping not only induces intrinsic defects, but also contributes massive electrons to the frameworks of the materials,[25,26] paving a new path to tailoring the band gaps,[27] oxygen vacancies,[28] as well as insulator-to-conductor transition.[29] Despite much progress, hydrogen doping remains a challenging issue to metal oxide semiconductors that usually require harsh reduction conditions (e.g., high temperatures and

Received: May 25, 2016
Published: July 6, 2016

ACS Publications © 2016 American Chemical Society

DOI: 10.1021/jacs.6b05396
J. Am. Chem. Soc. 2016, 138, 9316−9324

pressures),[25] and little is known about the potential that hydrogen doping might endow semiconductors with noble metal-comparable plasmonic feature, which enables them to harvest visible light energy to drive the subsequent catalytic reaction.

Herein, we report a facile H-spillover route to prepare heavily hydrogen-doped semiconductors, specifically hydrogen molybdenum bronzes (H_xMoO_3) and hydrogen tungsten bronzes (H_xWO_3). These hydrogen bronzes exhibit strong plasmonic absorption in the visible light spectrum, which is tunable in a wide range by varying their stoichiometry. Density functional theory (DFT) calculations reveal that the intercalating hydrogen atoms into the given host structures of MoO_3 and WO_3 could yield sufficient delocalized electrons to support their plasmon resonances. Under visible light, the plasmonic hybrids displayed superior catalytic activity toward *p*-nitrophenol reduction relative to dark condition.

2. RESULTS AND DISCUSSION

Schematic Illustration. To demonstrate a generalized strategy, commercially available MoO_3 (orthorhombic, microsized plates) and WO_3 (monoclinic, submicron particles) were employed as the starting materials (Figure S1). As illustrated in Scheme 1, synthesis of the corresponding hydrogen bronzes is based on the H-spillover process,[30−33] in which the chemisorbed hydrogen molecules dissociate at metal sites (e.g., Pd) to highly reactive hydrogen atoms, migrate to the surface of semiconductor supports, and further diffuse into the bulk, thereby leading to the reduction of the semiconductor. The H-spillover process was verified by hydrogen temperature-programmed reduction (H_2 TPR, Figure S2) results. Pure MoO_3 and WO_3 are hardly reduced by molecular H_2 below 400 and 550 °C, respectively; this is consistent with the previous study.[34] To verify this, pristine MoO_3 and WO_3 were reduced by H_2 at 300 °C in the absence of metal species, and almost no changes were observed from both X-ray diffraction (XRD) patterns and UV/vis−NIR diffuse reflectance spectra before and after H_2 reduction (Figure S3). However, the presence of a metal such as Pd enables MoO_3 and WO_3 to shift their reduction peaks toward lower temperatures, and thus MoO_3 and WO_3 could be reduced even at as low as room temperature (RT).[32,33] In addition, SiO_2 as the nonreducible oxide was also employed as support material to prepare the Pd/SiO_2 and Au/SiO_2 hybrids. Compared to MoO_3 and WO_3, less H_2 consumption and no correlative H_2 TPR peaks assigned to support were found in SiO_2 cases (Figure S2), further confirming the occurrence of H-spillover effect between metals and reducible metal oxides. The intercalation of hydrogen atoms into MoO_3 and WO_3 host structures will yield a class of H_xMoO_3 ($0 < x \leq 2$) and H_xWO_3 ($0 < x < 0.6$), along with partial reduction of metal ions.[35]

Scheme 1. Schematic Diagram of the Formation of Hydrogen Bronzes via H-Spillover Process

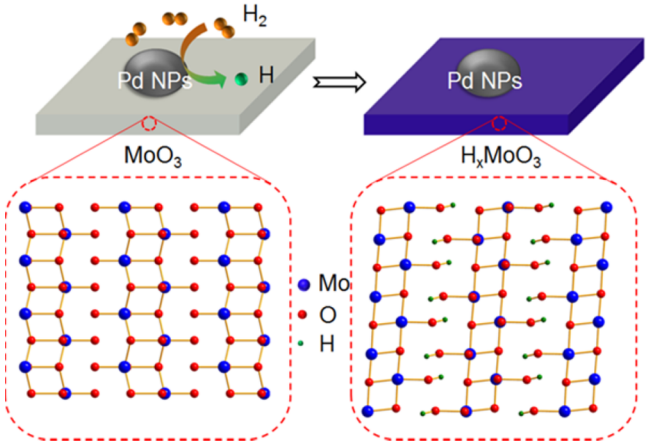

Structural Characterization. To check the effect of H-spillover, Pd/MoO_3 was first prepared by a wet impregnation method and further reduced by H_2 at ambient pressure. Figure 1a presents the UV/vis−NIR diffuse reflectance spectra of the products before and after H_2 reduction at RT. Before H_2 reduction, the Pd/MoO_3 hybrid only shows a slight absorption tail around 400 nm. In contrast, upon H_2 reduction at RT, the as-prepared product (denoted as Pd/MoO_3 H_2-RT) exhibits strong optical absorption in the visible regime, with an LSPR peak pinning at approximately 565 nm. XRD pattern of Pd/MoO_3 H_2-RT can be predominantly indexed to monoclinic $H_{1.68}MoO_3$ (PDF#33-0604), while scanning electron microscopy (SEM) and transmission electron microscopy (TEM) reveal that Pd nanoparticles (NPs) with an average size of 11.7 nm are anchored on the $H_{1.68}MoO_3$ microsized plates (Figure S4). By comparison with the UV/vis−NIR diffuse reflectance spectra of the Pd/SiO_2 hybrids before and after H_2 reduction at room temperature (Figure S5), the strong plasmonic band of the Pd/MoO_3 H_2-RT product arises from $H_{1.68}MoO_3$ through hydrogen doping. Notably, this short LSPR wavelength is exceptional and rare in doped semiconductors (Table S1) that usually appear in the near- to mid-infrared region, nearly comparable to noble metals (Table S2).

X-ray photoelectron spectroscopy (XPS) measurements were performed to determine the surface oxidation states of elements in the products. Figure 1b displays the XPS spectra of Mo 3*d* core level peaks in the Pd/MoO_3 products before and after H_2 reduction. It is observed that prior to H_2 reduction, only Mo^{6+} ions exist in Pd/MoO_3; however, after H_2 reduction at RT, Mo^{6+}, Mo^{5+}, and Mo^{4+} ions are all present in the product. Indeed, the Mo 3*d* core level spectrum of Pd/MoO_3 exhibits the characteristic spin−orbit doublet with binding energy (BE) peaks at 232.6 and 235.7 eV, correlating with $3d_{5/2}$ and $3d_{3/2}$ of Mo^{6+} species at higher oxidation state.[36] H_2 reduction renders the Mo 3*d* core level spectrum broader and less-structured, which could be further fitted into three overlapping spin−orbit doublets. Apart from Mo^{6+}, lower oxidation states of Mo species, that is, Mo^{5+} (BE at 230.8 and 234.0 eV) and Mo^{4+} (BE at 229.7 and 232.7 eV) ions also appear.[37] By analyzing the corresponding area of peaks assigned, it is revealed that Mo^{6+}, Mo^{5+}, and Mo^{4+} ions account for approximately 24%, 57%, and 19%, respectively. To further elucidate the local structure change of MoO_3 support during H_2 reduction, X-ray absorption fine structure (XAFS) measurements were conducted. In Figure 2c of the normalized X-ray absorption near-edge structure (XANES) spectra, the line shapes at the edge differentiate the assignment of Mo species. As expected, Mo foil has the lowest absorption edge, followed by the Pd/MoO_3 H_2-RT product, whereas MoO_3 and Pd/MoO_3 have the highest absorption edges. Additionally, a pre-edge feature of MoO_3 with Mo^{6+} oxidation state is absent in the case of the product of Pd/MoO_3 H_2-RT, which demonstrates that the Pd/MoO_3 H_2-RT locates between Mo foil and MoO_3. Figure 2d presents the Fourier-transformed extended XAFS (FT-EXAFS) spectra for Mo *K*-edge (k^3-weighted in *k* space) of the samples. In Mo foil, the

DOI: 10.1021/jacs.6b05396
J. Am. Chem. Soc. 2016, 138, 9316−9324

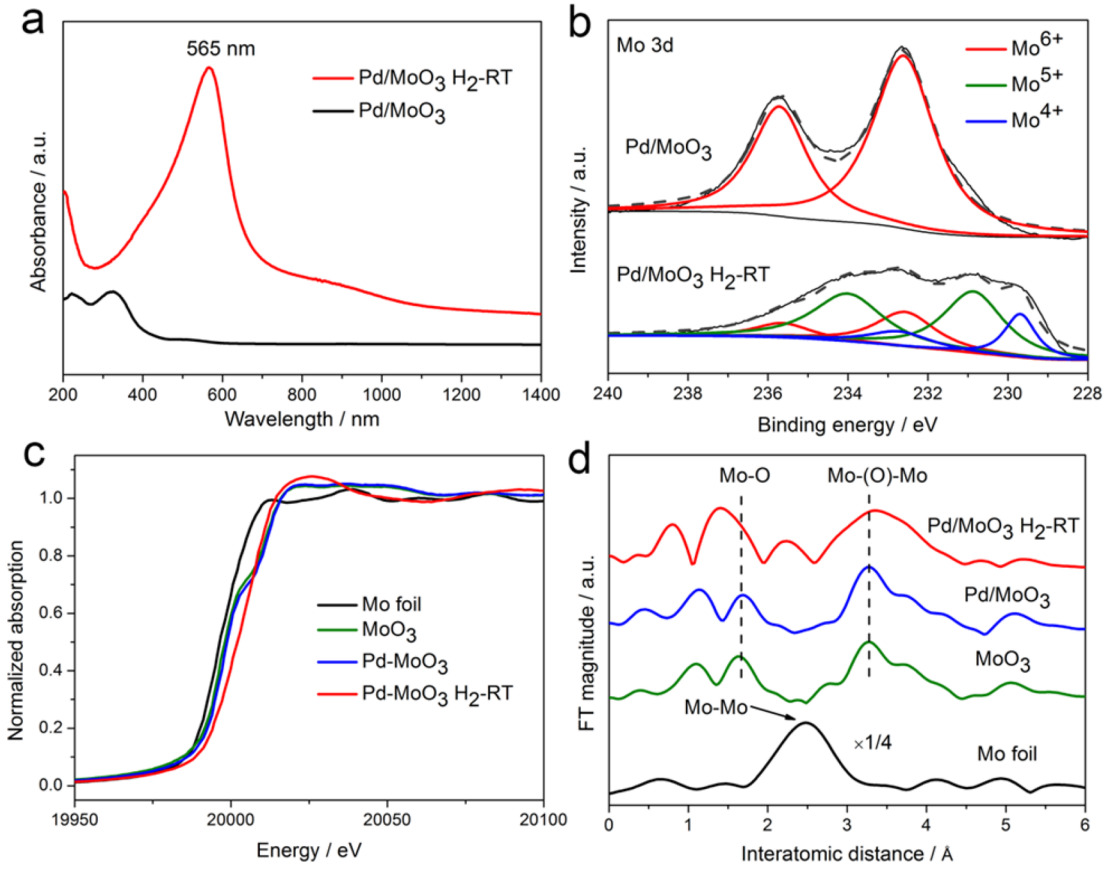

Figure 1. Optical and structural characterizations of hydrogen molybdenum bronze. (a) UV/vis−NIR diffuse reflectance spectra and (b) Mo 3*d* XPS spectra of Pd/MoO_3 products before and after H_2 reduction at room temperature. (c) Mo *K*-edge XANES and (d) FT-EXAFS spectra for the Pd/MoO_3 products before and after H_2 reduction and the reference materials (Mo foil and MoO_3).

predominant peak at approximately 2.5 Å is assigned to Mo−Mo bonding. In MoO_3 and the Pd/MoO_3 products before and after H_2 reduction, the peaks at around 1.5 Å is due to Mo−O bond in the MoO_6 octahedra, while the peaks at around 3.5 Å is attributed to Mo−(O)−Mo bonding.[38] Different from MoO_3 and Pd/MoO_3, a new peak around 2.3 Å appears in the Pd/MoO_3 H_2-RT hybrid that is attributed to Mo−Mo bonding between two edge-sharing MoO_6 octahedra.[38] Through heavily hydrogen intercalation assisted by H-spillover process, the MoO_6 octahedra in MoO_3 become more distorted, enabling the transition of the semiconducting MoO_3 to metallic $H_{1.68}MoO_3$. In addition, Pd element was also studied by XPS (Figure S6) and XAFS (Figure S7) measurements. Both of the results reveal that prior to H_2 reduction, the Pd species in the Pd/MoO_3 existed mainly in the form of Pd^{2+}, while after H_2 reduction at RT, the Pd species were fully reduced to metallic Pd^0.

Tunable Surface Plasmon Resonances. In our study, the plasmonic property of the hydrogen bronzes is found to be closed related to their stoichiometric compositions, which further depends on the parameters variation in the synthetic process as well as oxidation treatment in the postsynthetic process. Figure 2a shows the UV/vis−NIR diffuse reflectance spectra of the Pd/MoO_3 products on H_2 reduction at different temperatures. When H_2 reduction temperature of Pd/MoO_3 was varied from RT to 100 and 200 °C, a red shift of the plasmonic wavelength from 565 to 588 nm was observed, along with the wider absorption peaks. During this process, the corresponding structural changes were checked by the XRD patterns (Figure 2b). With the rise of reduction temperature, the relative proportion of $H_{1.68}MoO_3$ decreased while that of $H_{0.9}MoO_3$ increased. It is thus indicated that $H_{1.68}MoO_3$ is gradually transformed to $H_{0.9}MoO_3$ at elevated temperatures, and their plasmonic wavelength shifts to longer wavelength due to the decrease of free electrons concentration. Nonetheless, further rise of reduction temperature to 300 °C leads to the quenching of plasmonic absorption in the product, of which the structure are largely decomposed into amorphous MoO_2 (Figure S8).

Apart from Pd, other metal species such as Au are also able to tailor the surface plasmon resonances of hydrogen bronzes through H-spillover process. Due to LSPR of Au NPs, Au/MoO_3 exhibits a slight absorption peak around 580 nm (Figure 2c). After H_2 reduction, the Au/MoO_3 H_2-200 °C product displays strong visible light response with an absorption peak pinning at 582 nm. This product is predominantly assigned to $H_{1.68}MoO_3$, with metallic Au NPs of around 28 nm on the support material (Figure S9). As confirmed by XAFS (Figure S9) and XPS (Figure S10) measurements, Au species are in the form of metallic Au^0, regardless of H_2 reduction treatment of the Au/MoO_3 products or not. Temperature-dependence was also found in the optical absorption of the Au/MoO_3 products upon H_2 reduction (Figure S11). In contrast to Pd/MoO_3, higher temperature of H_2 reduction is required for Au/MoO_3 to achieve plasmonic absorption in the final products. This arises from the fact that Pd NPs dissociates H_2 with lower activation energy than Au NPs,[30] and consequently higher reduction temperature is required to surmount the energy barrier in the case of Au/MoO_3.

DOI: 10.1021/jacs.6b05396
J. Am. Chem. Soc. 2016, 138, 9316−9324

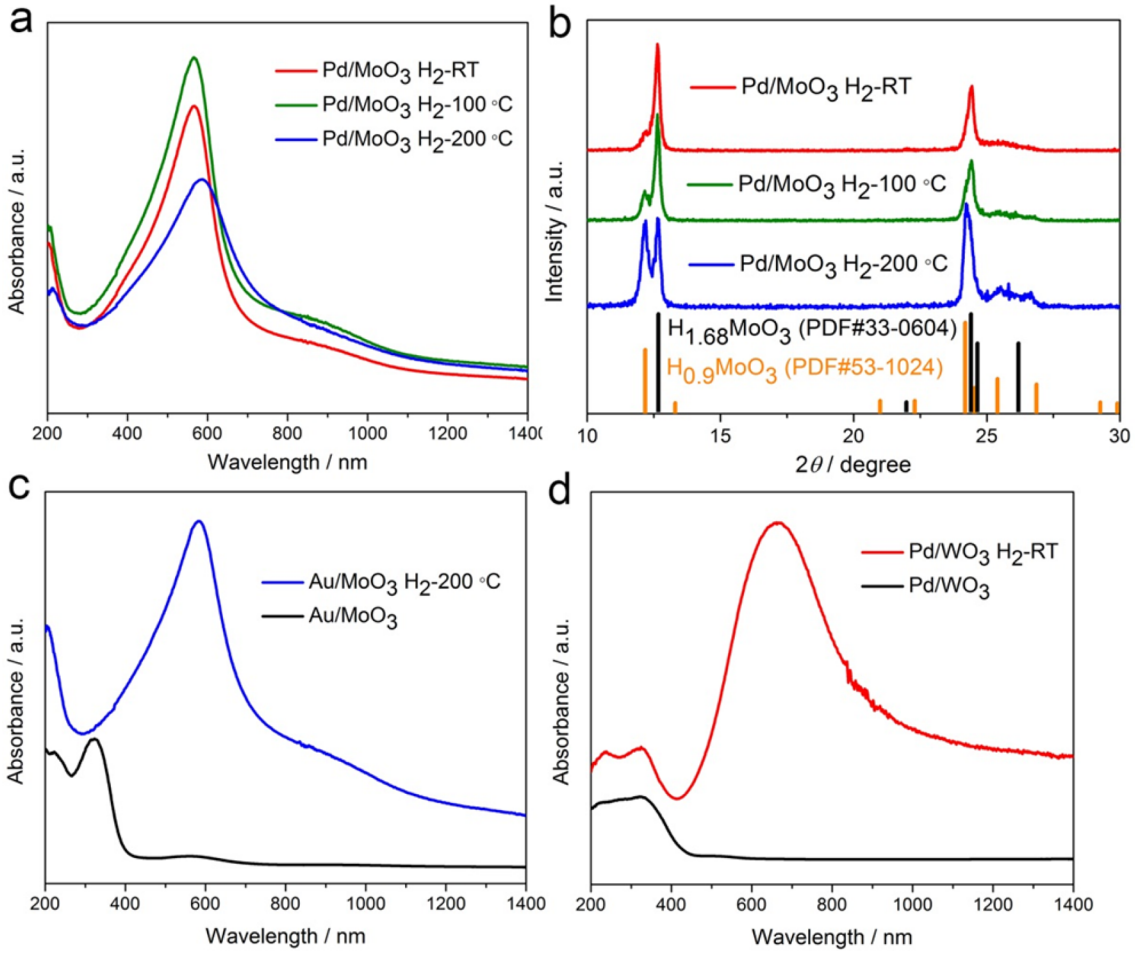

Figure 2. Tunable plasmon resonance in hydrogen bronzes. (a) UV/vis−NIR diffuse reflectance spectra and (b) XRD patterns of the Pd/MoO_3 samples upon H_2 reduction at different temperatures. The drop lines show the standard pattern of monoclinic $H_{1.68}MoO_3$ (black, PDF#33-0604) and monoclinic $H_{0.9}MoO_3$ (orange, PDF#53-1024). (c) UV/vis−NIR diffuse reflectance spectra of Au/MoO_3 samples before and after H_2 reduction at 200 °C. (d) UV/vis−NIR diffuse reflectance spectra of Pd/WO_3 samples before and after H_2 reduction at room temperature.

Additionally, the surface plasmon resonance of hydrogen bronzes is also associated with the nature of the support materials. Besides H_xMoO_3, Pd/WO_3 was also prepared to investigate H_xWO_3 through H-spillover. As shown in Figure 2d, with an absorption edge around 450 nm, Pd/WO_3 does not display optical response at longer wavelength. Upon H_2 reduction, the Pd/WO_3 H_2-RT product exhibits intense optical absorption in the visible light to NIR region, with an LSPR peak pinning at around 660 nm. With Pd NPs having mean size of 11 nm on the support material, the Pd/WO_3 H_2-RT product is well assigned to tetragonal $H_{0.33}WO_3$ (PDF#23-1449, Figure S12). Different from the cases of Pd/MoO_3 and Au/MoO_3, the structure of $H_{0.33}WO_3$ can be maintained in a wide reduction temperature range (from RT to 300 °C), and thus there are slight changes in plasmonic absorption of the Pd/WO_3 products upon H_2 reduction (Figure S13).

Furthermore, the size of support material also plays an important role in tuning the plasmonic resonances of the hydrogen bronzes. To this end, MoO_3 nanosheets[20] were also employed as the support material to the resulting H_xMoO_3 through H_2 reduction of the Pd/MoO_3 nanosheets hybrid (Figure S14). Upon H_2 reduction, plasmonic absorption of the Pd/MoO_3 nanosheets hybrid was also observed, but with red shift compared to the Pd/MoO_3 hybrid using commercial MoO_3. As commercial MoO_3 possesses smaller surface area (1.7 m^2/g) than MoO_3 nanosheets (25 m^2/g), migration of H atoms from surface into bulk would be important to achieve higher hydrogen content in the H_xMoO_3, thereby enabling their stronger plasmonic resonances at shorter wavelengths.

Unlike noble metals, one unique feature of highly doped semiconductors is that their plasmonic resonance is closely related to the oxidation/reduction process.[19,21] When exposed to air condition, oxidation of the hydrogen bronzes will lead to the red shift of their plasmonic absorption. Through gradual oxidation by O_2 in air, optical absorption of the Pd/WO_3 H_2-300 °C product evolved from a narrow band at 640 nm to a broader peak at 780 nm in 1 h, and finally the absorption peak vanished within 4 h (Figure S15). This fast decay process of plasmon resonance of H_xWO_3 is correlated with its structural variation, which was transformed completely into WO_3 upon oxidation for 4 h. In contrast, H_xMoO_3 undergoes slower decay process of surface plasmon. After 24 h of air exposure, the Pd/MoO_3 H_2-RT product still showed an LSPR peak pinning at about 620 nm, accompanying the structure variation from $H_{1.68}MoO_3$ to $H_{0.34}MoO_3$ (Figure S16). The loss of hydrogen content in support materials decreases the free electrons concentration injected, and thus causes red shift of their plasmonic absorption.

Free Carrier Density Calculations. The surface plasmon resonance in hydrogen bronzes correlates with their abundant

DOI: 10.1021/jacs.6b05396
J. Am. Chem. Soc. 2016, 138, 9316−9324

free electrons, and can be described by the Drude model,[13] where complex dielectric function, ε, of the plasmonic material expressed as a function of the light frequency, ω.

$$\varepsilon(\omega) = \varepsilon_1 + i\varepsilon_2 = \varepsilon_b - \frac{{\omega_p}^2}{\omega^2 + \gamma^2} + i\frac{{\omega_p}^2\gamma}{\omega(\omega^2 + \gamma^2)} \quad (1)$$

Here ε_1 and ε_2 are the real and imaginary parts, respectively, of the material, ε_b is the polarization response from the core electrons (background permittivity) and usually equals to 1, ω_p is the bulk plasma, and γ is the damping parameter that numerically equals to the line width of the plasmon resonance band.[39,40] At the resonance condition, the LSPR frequency ω_{sp} can be expressed as

$$\omega_{sp} = \sqrt{\frac{{\omega_p}^2}{1 + 2\varepsilon_m} - \gamma^2} \quad (2)$$

where ε_m is the dielectric constant of the surrounding medium. In our case, the optical spectra of the samples were measured in air condition, and thus, the value of ε_m is 1. For the Pd/MoO_3 H_2-RT product, it shows the resonance energy ω_{sp} of 2.19 eV at the LSPR wavelength (565 nm), and the line width of 0.17 eV by measuring the full width at half-maximum (fwhm) of the optical spectrum (Figure S17). Consequently, the bulk plasma frequency ω_p is approximately estimated to be 3.80 eV. Moreover, the bulk plasma frequency ω_p depends on the free electrons density N by the formula

$${\omega_p}^2 = \frac{Ne^2}{\varepsilon_0 m^*} \quad (3)$$

where e is the elementary charge, ε_0 is the permittivity of free space, and m^* is the effective mass of the free carriers. According to DFT calculations, the effective electron masses of MoO_3 and WO_3 are calculated to be $m^* = 0.55m_0$ and $m^* = 0.4m_0$, respectively, where m_0 is the electron rest mass. Therefore, the free electron concentration N is estimated to be 5.8×10^{21} cm^{-3} in the Pd/MoO_3 H_2-RT product. The parameters of the plasmonic hydrogen bronzes are summarized in Table 1.

Table 1. Parameters of Plasmonic Hydrogen Bronzes

samples	λ_{LSPR} (nm)	γ (eV)	ω_p (eV)	N (cm^{-3})
Pd/MoO_3 H_2-RT	565	0.17	3.80	5.8×10^{21}
Pd/MoO_3 H_2-100 °C	565	0.18	3.81	5.8×10^{21}
Pd/MoO_3 H_2-200 °C	588	0.28	3.69	5.4×10^{21}
Au/MoO_3 H_2-200 °C	582	0.25	3.71	5.5×10^{21}
Pd/WO_3 H_2-RT	660	0.29	3.29	3.1×10^{21}

DFT Calculations. To reveal the origin of surface plasmon resonance in the hydrogen bronzes and understand the drastic changes induced by hydrogen doping process, we systematically studied the electronic structures of the hydrogen bronzes by first-principles DFT calculations. Figure 3a presents the total density of states (TDOS) and projected density of states (PDOS) of pristine MoO_3. Clearly, no defect states are present in pristine MoO_3, and the bandgap between valence band (VB) and conduction band (CB) is approximately 1.9 eV. As compared to pristine MoO_3 that has semiconductor-like band structure, heavily doped hydrogen molybdenum bronze ($H_{1.68}MoO_3$) displays strong metallic feature with continuous VB across the Fermi level into the CB (Figure 3b). The drastic changes in electronic structures of hydrogen molybdenum bronzes stems from the intercalation of hydrogen atoms into the MoO_3 matrix and subsequent charge transfer. With corner- and edge-sharing MoO_6 octahedra, the layered structure of orthorhombic MoO_3 host material allows massive H atoms insertion at interlayer positions, which coordinate strongly with terminal oxygen atoms and lead to the distortion of MoO_6 octahedra in the resultant $H_{1.68}MoO_3$ framework (Figures 3c and S18). Upon adsorption on terminal oxygen atoms, hydrogen atoms become protonic and electron transfer from H 1*s* orbital to the O 2*p* orbital takes place.[41] Subsequently, the terminal oxygen atoms transfer charges to the coordinating Mo atoms, thereby leading to partial reduction of molybdenum ions and shortening of Mo−O bonds; this is in good line with XPS and XAFS experimental results (Figure 1). From the three-dimensional (3D) visualization of electronic charge density distribution for $H_{1.68}MoO_3$ (Figure 3d), it is seen that the introduced electronic charge is distributed uniformly on Mo atoms, indicative of the delocalization nature of Mo 4*d* electrons. According to the band structure models proposed by Goodenough,[42] it is reasonable to accept that Mo 4*d* orbitals of t_{2g} symmetry overlap with the intermediary O $2p_\pi$ orbitals to yield a partially filled π^* band, shifting their Fermi level within the CB. With such high degree of delocalization, free electrons donated by hydrogen atoms are expected to, when exceeding the critical concentration, support the observed LSPR in the visible light spectrum.

In H_xMoO_3, H atoms reside in interlayer positions and coordinate with terminal O atoms, and the donated electrons are fully delocalized; however, that is not the case in H_xWO_3. Monoclinic WO_3 crystallizes in distorted ReO_3-type structure with corner-sharing WO_6 octahedra, and the inserted H atoms verify the W−O−W angles and reside in the tunnels in H_xWO_3 ($H_{0.5}WO_3$ as a case study, Figure S19). In contrast to pristine WO_3 with semiconducting band diagram, $H_{0.5}WO_3$ displays a large peak at the bottom of the CB and the Fermi level is positioned near the middle of this sub-band (Figure S20). This band is attributed to the nonionized H 1*s* orbital, and only one electron is contributed from the hydrogen.[43] As a consequence, partial protonation of H atoms provides considerable collective electrons, supporting the LSPR property of hydrogen tungsten bronzes. Additionally, in contrast to hydrogen molybdenum bronzes where H atoms reside in the interlayer sites of MoO_3 and bound to terminal O at oms, H atoms reside in the tunnel sites of WO_3 in hydrogen tungsten bronzes, which are more unstable to extract from the host structure and explains why they display much faster decay process of plasmon resonance.

The coordination environment of hydrogen atoms and the delocalization extent of the electrons determine the electronic properties of hydrogen bronzes, and further their corresponding optical properties. As another host material, the crystal structure of orthorhombic V_2O_5 consists of VO_5 square base pyramidal units linked by corner and edge sharing, and H atoms could occupy the interstitial sites available between the layers in $H_xV_2O_5$ (in the case of $H_{0.5}V_2O_5$, Figure S21). With respect to V_2O_5, $H_{0.5}V_2O_5$ just shows defect state due to V below the Fermi level in the band diagram (Figure S22). These defect states are ascribed to V^{4+} and V^{3+} paramagnetic centers,[44,45] which originate from the localized electrons provided by the inserted H atoms. To verify whether these localized electrons could support the surface plasmon resonance or not, we have also prepared hydrogen vanadium bronzes ($H_xV_2O_5$) from Pd/V_2O_5 through H-spillover process

DOI: 10.1021/jacs.6b05396
J. Am. Chem. Soc. 2016, 138, 9316−9324

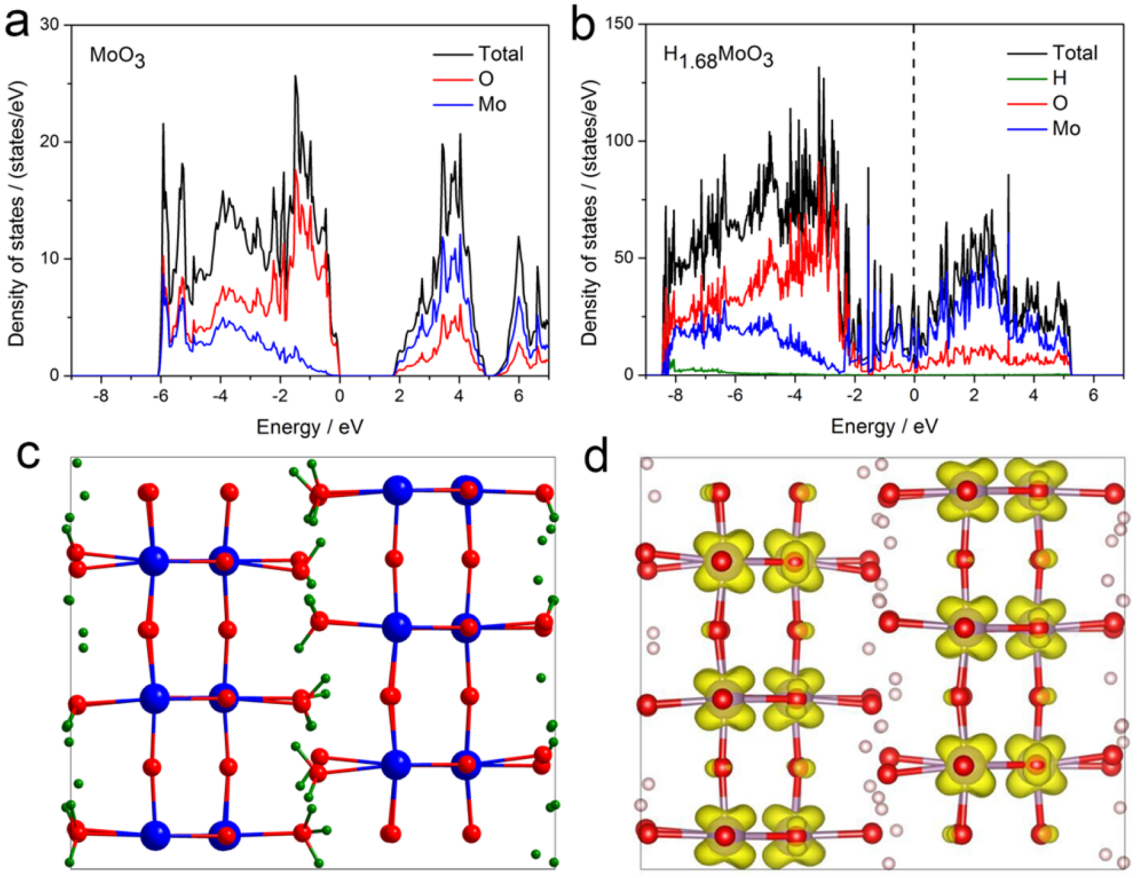

Figure 3. Density functional theory calculations. TDOS and PDOS of (a) pure MoO_3 and (b) heavily hydrogen-doped $H_{1.68}MoO_3$. (c) Structure illustration for $H_{1.68}MoO_3$ in (010) projection. Blue balls represent Mo atoms, red for O, and green for H atoms. (d) Three-dimensional visualization of electronic charge density distribution around the Fermi level for $H_{1.68}MoO_3$.

at room temperature. No plasmonic absorption was observed in the final product (Figure S23), which further elucidates that the confined electrons in hydrogen vanadium bronzes fail to support their plasmon resonance.

Catalytic Applications. Through a facile H-spillover process, it gives rise to Pd NPs supported on the plasmonic H_xMoO_3 materials, allowing the investigation of their application in heterogeneous catalysis. We adopted the reduction of *p*-nitrophenol (4-NP) to *p*-aminophenol (4-AP) as a model reaction[46,47] to evaluate their catalytic activity, where ammonia borane (AB, NH_3BH_3) as a novel and mild H_2 source was chosen to replace the unstable and toxic $NaBH_4$ agent.[48] The 4-NP solution exhibits a major absorption peak at 317 nm under neutral condition, and upon addition of AB solution it shifts to 400 nm in the presence of Pd/MoO_3 H_2-RT catalyst. As shown in Figure 4a,b, with reaction time proceeding, the absorption peak of 4-NP at 400 nm gradually decreased in intensity both in the dark and under visible light ($\lambda > 420$ nm) conditions. From the plots of absorbance at 400 nm as a function of reaction time (Figure 4c), it is clearly seen that the catalytic performance of the Pd/MoO_3 H_2-RT under visible light irradiation is superior to that in the dark condition. Without catalysts, the absorption peaks of 4-NP at 400 nm did not decrease but rather increased, in either dark or visible light conditions (Figure S24). The results show that in the absence catalysts, reduction of 4-NP to 4-AP could not take place, and NH_3BH_3 is quite stable, with its weak dehydrogenation increasing the alkalinity of the solution slowly. Assuming the reduction reaction of 4-NP proceeds with the pseudo-first-order kinetics, we applied the plot of $-\ln(C/C_0)$ versus reaction time (Figure 4d). In dark condition, the reaction shows the quasi-linear shape with the average reaction rate constant (k) of 0.014 min^{-1}; whereas under visible light irradiation, the reaction displays nonlinear shape and the initial reaction k (in the first 30 min) is around 0.039 min^{-1}, which is 2.8 times that in the dark condition. Visible light induced enhancement in the catalytic activity of Pd/MoO_3 H_2-RT is considered to be related to the plasmonic effect of hydrogen molybdenum bronzes. Under visible light, plasmonic hydrogen molybdenum bronze is excited to yield hot energetic electrons that transfer to the contiguous Pd NPs, thereby facilitating the interfacial charge transfer.[6,49] In this way, the surfaces of Pd NPs were negatively charged and H_xMoO_3 supports were positively charged, which facilitated the catalytic reactions of NH_3BH_3 hydrogenation and the subsequent 4-NP reduction on Pd NPs. Notably, such enhancement in catalysis was obtained with large Pd NPs (~11.7 nm), suggesting the potentials to drive chemical reactions with noble-metal-comparable plasmonic doped-semiconductor materials, and it is anticipated to achieve higher catalytic performances by careful combination of the plasmonic hydrogen bronzes and ultrafine metal NPs.

3. CONCLUSIONS

In summary, hydrogen molybdenum bronzes and hydrogen tungsten bronzes, a class of heavily hydrogen-doped semiconductors, were prepared via H-spillover process. They exhibit

DOI: 10.1021/jacs.6b05396
J. Am. Chem. Soc. 2016, 138, 9316−9324

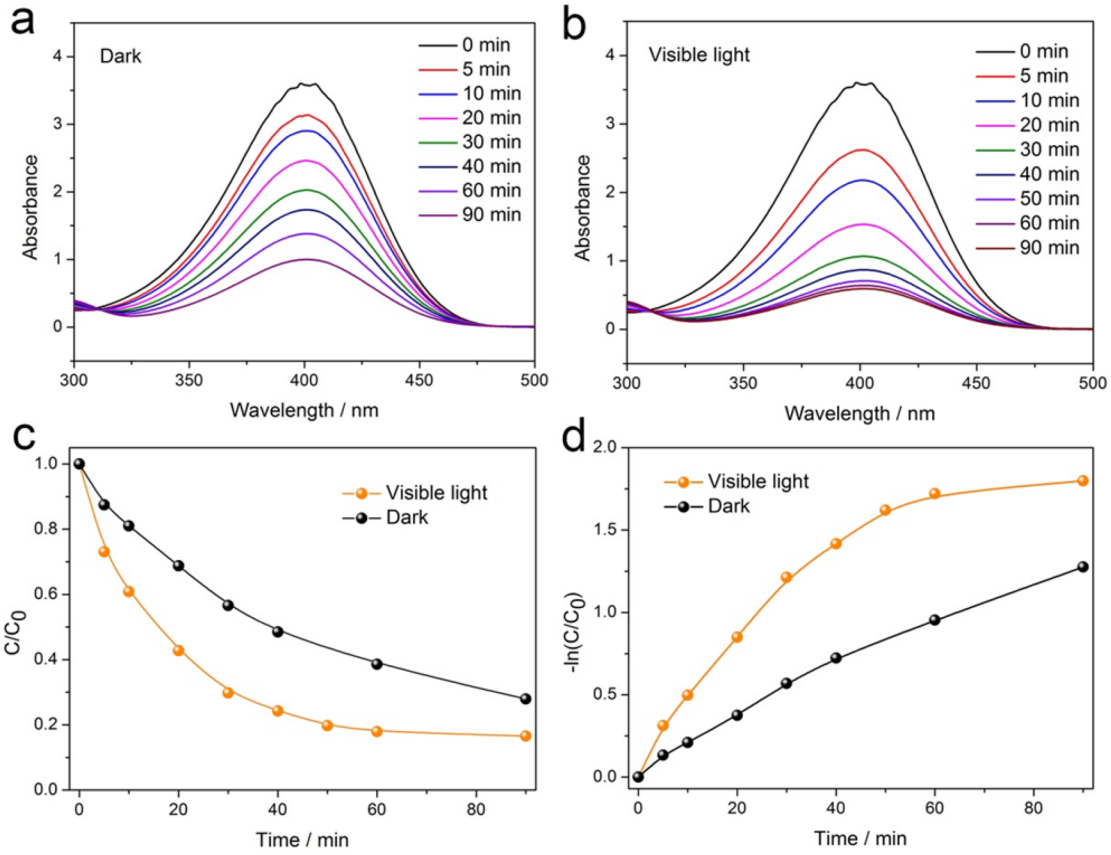

Figure 4. Catalytic properties of Pd/MoO_3 H_2-RT products in the dark and under visible light irradiation. Time-dependent evolution of UV/vis absorption spectra of reaction solutions over Pd/MoO_3 H_2-RT catalyst (a) in the dark and (b) under visible light irradiation (λ > 420 nm). (c) Plots of absorption against the initial point at 400 nm peak for 4-NP as a function of time and (d) corresponding plots of $-\ln(C/C_0)$ versus time that are generated from (c).

strong visible light plasmon resonances, which could be tuned in a wide range through variation of their stoichiometry. Theoretical calculations indicate that hydrogen doping into MoO_3 and WO_3 yields appreciable delocalized electrons, enabling their exceptional plasmonic properties; whereas it leads to confined electrons in other metal oxides such as V_2O_5, failing to sustain surface plasmons. In contrast to dark condition, the plasmonic support boosts Pd-catalyzed reduction of *p*-nitrophenol upon exposure to visible light. This work extends the window of visible-light-responsive plasmonic materials of doped semiconductors, and we believe their coupling with ultrafine metal nanoparticles will find more efficient applications in biomedicine, gas sensing, and so on.

4. EXPERIMENTAL SECTION

Chemicals. All the chemical agents were used as received unless otherwise noted. MoO_3 and WO_3 were purchased from Wako Pure Chemical Industries, Ltd. V_2O_5, $PdCl_2$, $HAuCl_4$, HCl, ethanol, and 4-NP were obtained from Nacalai Tesque Inc. NH_3BH_3 (AB) and fumed SiO_2 were obtained from Sigma-Aldrich. H_2PdCl_4 (6.767 mM) solution was obtained by dissolving 0.6 g of $PdCl_2$ with 3 mL of HCl (5 M) solution and further diluted with distilled water to a final volume of 500 mL.

Synthesis. A two-step synthetic process was adopted to prepare the hydrogen doped semiconductors. Taking Pd/MoO_3, for example, first, Pd/MoO_3 (2 wt %) was obtained by conventional wet impregnation method. MoO_3 (1 g) was dispersed in 100 mL of distilled water containing certain amount of H_2PdCl_4 solution, which was stirred vigorously overnight, evaporated by a vacuum rotary evaporator at 60 °C, fully dried at 100 °C, and then calcined in air at 300 °C for 2 h with the ramping rate of 5 °C/min. Second, hydrogen reduction of Pd/MoO_3 was conducted with pure H_2 gas at ambient pressure (1 bar). The products prepared at different reduction temperatures were termed as Pd/MoO_3 H_2-T (T means the temperature). The heating rate is 5 °C/min, and the sample was kept at the final temperature for 1 h. Analogously, other hydrogen bronzes hybrids were also prepared by hydrogen reduction of Au/MoO_3, Pd/WO_3 or Pd/V_2O_5 with the method mentioned above. For comparison, pristine MoO_3 and WO_3 were reduced by H_2 at 300 °C for 1 h in the absence of metal species. To check the support effect, Pd/SiO_2 hybrids before and after H_2 reduction at room temperature were also prepared.

Characterizations. XRD pattern was recorded on a Rigaku RINT2500 diffractometer with Cu Kα radiation (λ = 1.5406 Å). Nitrogen sorption analysis was performed at 77 K using a QUADRASORB SI device manufactured by Quantachrome, and surface area was determined by the Brunauer–Emmett–Teller (BET) method. Before measurement, samples were degassed at 120 °C for 20 h. SEM images were taken using a JEOL JSM-6500 field emission microscope. TEM images were obtained on a FEI Tecnai G^2 20 S-TWIN electron microscope operated at 200 kV. UV/vis–NIR diffuse reflectance spectra were collected on a Shimadzu UV-2600 recording spectrophotometer equipped with an integrating sphere. $BaSO_4$ was employed as the reference, and the absorption spectra were obtained by using the Kubelka–Munk function. XPS measurements were carried out using a Shimadzu ESCA 3400 photoelectron spectrometer with Mg Kα radiation, and C 1*s* (284.8 eV) was used to calibrate the binding energies of the elements. Au L_{III}-edge and Pd *K*-edge XAFS measurements were performed at the beamline BL01B1 station in fluorescence mode with an attached Si(111) monochromator at SPring-8, Harima, Japan (Prop. No. 2015A1149 and 2015B1083). Mo

DOI: 10.1021/jacs.6b05396
J. Am. Chem. Soc. 2016, 138, 9316–9324

K-edge XAFS measurements were performed in the fluorescence mode at the BL-9C facilities of the Photon Factory at the High Energy Accelerator Research Organization (KEK) in Tsukuba, Japan (Prop. No. 2015G025). The synchrotron radiation from a 2.5 GeV electron storage ring was monochromatised by an Si(311) double crystal. The EXAFS data were normalized by fitting the background absorption coefficient using the Rigaku EXAFS analysis program. The FT-EXAFS data was performed over the $3.0 < k/Å^{-1} < 12.0$ range to obtain the radial structure function. H_2 TPR measurement was carried out on a BELCAT-II (MicrotracBEL Corp.) apparatus. The samples were mounted in a quartz tube, and were reduced in a flow of 5 vol % H_2/Ar (30 mL/min). The heating rate of 5 °C/min, and the consumption of hydrogen was monitored by the thermal conductive detector (TCD).

Theoretical Calculations. The DFT calculations are conducted using the Vienna Ab initio Simulation Package code.[50] The ionic potentials are described by the projector augmented wave (PAW) method[51,52] within the generalized gradient approximation (GGA).[53] The plane wave cutoff energy is 400 eV. For all systems, both the lattice vector and atomic positions are fully relaxed until the residual Hellmann−Feynman forces become smaller than 0.02 eV/Å. The electron effective mass is calculated by parabolic fitting the curvature around the conduction band minimum (CBM) of respective system.

Catalytic Activity. The catalytic activity of Pd NPs supported hydrogen molybdenum bronzes was evaluated by reduction of 4-NP to 4-AP by AB at room temperature. The Pd/MoO_3 H_2-RT product (5 mg) was suspended in 30 mL of 4-NP (0.2 mM) in a Pyrex glass tube. After bubbling with Ar gas for 30 min, 3 mL of the freshly prepared AB (0.1 M) solution was injected into the suspension through a rubber septum by using a syringe. The reaction was carried out with magnetic stirring in the dark or under visible light irradiation ($\lambda > 420$ nm) conditions. At given time intervals, 3 mL of the suspension was extracted and immediately passed through the syringe filter to the quartz cuvette. The reaction was monitored by measuring the intensity of the absorption band at 400 nm for 4-NP with a Shimadzu UV-2450 UV−vis spectrophotometer.

■ ASSOCIATED CONTENT

Supporting Information

The Supporting Information is available free of charge on the ACS Publications website at DOI: 10.1021/jacs.6b05396.

Extended characterization results, tables, and DFT calculations (PDF)

■ AUTHOR INFORMATION

Corresponding Authors

*yamashita@mat.eng.osaka-u.ac.jp

*bbhuang@sdu.edu.cn

Present Address

#School of Physics and Optoelectronic Engineering, Xidian University, Xi'an 710071, China.

Author Contributions

⊥H.C. and M.W. contributed equally to this work.

Notes

The authors declare no competing financial interest.

■ ACKNOWLEDGMENTS

The present work was supported by the Grant-in-Aid for Scientific Research from the Ministry of Education, Culture, Sports, Science and Technology (MEXT) of Japan (26620194 and 26220911). Part of this work was performed under a management of "Elements Strategy Initiative for Catalysts and Batteries (ESICB)" supported by MEXT program, Japan. H.C. would like to thank Japan Society for the Promotion of Science (JSPS) for the fellowship. Y.D. and B.H. acknowledge the National Basic Research program of China (973 program, 2013CB632401), the National Science Foundation of China (21333006) and the Taishan Scholar Program of Shandong.

■ REFERENCES

(1) Weiner, J.; Ho, P.-T. *Light-Matter Interaction: Fundamentals and Applications*; John Wiley & Sons: Hoboken, NJ, 2003.

(2) Naik, G. V.; Shalaev, V. M.; Boltasseva, A. *Adv. Mater.* **2013**, *25*, 3264.

(3) Lu, X.; Rycenga, M.; Skrabalak, S. E.; Wiley, B.; Xia, Y. *Annu. Rev. Phys. Chem.* **2009**, *60*, 167.

(4) Nie, S. M.; Emery, S. R. *Science* **1997**, *275*, 1102.

(5) Jain, P. K.; Huang, X.; El-Sayed, I. H.; El-Sayed, M. A. *Plasmonics* **2007**, *2*, 107.

(6) Linic, S.; Christopher, P.; Ingram, D. B. *Nat. Mater.* **2011**, *10*, 911.

(7) Chen, H. J.; Shao, L.; Li, Q.; Wang, J. F. *Chem. Soc. Rev.* **2013**, *42*, 2679.

(8) Tanaka, A.; Hashimoto, K.; Kominami, H. *J. Am. Chem. Soc.* **2012**, *134*, 14526.

(9) Mubeen, S.; Lee, J.; Singh, N.; Kramer, S.; Stucky, G. D.; Moskovits, M. *Nat. Nanotechnol.* **2013**, *8*, 247.

(10) Fuku, K.; Hayashi, R.; Takakura, S.; Kamegawa, T.; Mori, K.; Yamashita, H. *Angew. Chem., Int. Ed.* **2013**, *52*, 7446.

(11) Mori, K.; Kawashima, M.; Che, M.; Yamashita, H. *Angew. Chem., Int. Ed.* **2010**, *49*, 8598.

(12) Wang, P.; Huang, B.; Qin, X.; Zhang, X.; Dai, Y.; Wei, J.; Whangbo, M. *Angew. Chem., Int. Ed.* **2008**, *47*, 7931.

(13) Comin, A.; Manna, L. *Chem. Soc. Rev.* **2014**, *43*, 3957.

(14) Liu, X.; Swihart, M. T. *Chem. Soc. Rev.* **2014**, *43*, 3908.

(15) Kanehara, M.; Koike, H.; Yoshinaga, T.; Teranishi, T. *J. Am. Chem. Soc.* **2009**, *131*, 17736.

(16) Buonsanti, R.; Llordes, A.; Aloni, S.; Helms, B. A.; Milliron, D. J. *Nano Lett.* **2011**, *11*, 4706.

(17) Ye, X. C.; Fei, J. Y.; Diroll, B. T.; Paik, T.; Murray, C. B. *J. Am. Chem. Soc.* **2014**, *136*, 11680.

(18) Luther, J. M.; Jain, P. K.; Ewers, T.; Alivisatos, A. P. *Nat. Mater.* **2011**, *10*, 361.

(19) Manthiram, K.; Alivisatos, A. P. *J. Am. Chem. Soc.* **2012**, *134*, 3995.

(20) Cheng, H.; Kamegawa, T.; Mori, K.; Yamashita, H. *Angew. Chem., Int. Ed.* **2014**, *53*, 2910.

(21) Cheng, H.; Qian, X.; Kuwahara, Y.; Mori, K.; Yamashita, H. *Adv. Mater.* **2015**, *27*, 4616.

(22) Alsaif, M. M. Y. A.; Latham, K.; Field, M. R.; Yao, D. D.; Medehkar, N. V.; Beane, G. A.; Kaner, R. B.; Russo, S. P.; Ou, J. Z.; Kalantar-zadeh, K. *Adv. Mater.* **2014**, *26*, 3931.

(23) Boltasseva, A.; Atwater, H. A. *Science* **2011**, *331*, 290.

(24) Lounis, S. D.; Runnerstrom, E. L.; Llordes, A.; Milliron, D. J. *J. Phys. Chem. Lett.* **2014**, *5*, 1564.

(25) Sun, X.; Guo, Y. Q.; Wu, C. Z.; Xie, Y. *Adv. Mater.* **2015**, *27*, 3850.

(26) Ma, X.; Dai, Y.; Yu, L.; Huang, B. *Sci. Rep.* **2014**, *4*, 3896.

(27) Chen, X. B.; Liu, L.; Yu, P. Y.; Mao, S. S. *Science* **2011**, *331*, 746.

(28) Kim, J.; Yin, X.; Tsao, K. C.; Fang, S. H.; Yang, H. *J. Am. Chem. Soc.* **2014**, *136*, 14646.

(29) Kobayashi, Y.; Hernandez, O. J.; Sakaguchi, T.; Yajima, T.; Roisnel, T.; Tsujimoto, Y.; Morita, M.; Noda, Y.; Mogami, Y.; Kitada, A.; Ohkura, M.; Hosokawa, S.; Li, Z. F.; Hayashi, K.; Kusano, Y.; Kim, J. E.; Tsuji, N.; Fujiwara, A.; Matsushita, Y.; Yoshimura, K.; Takegoshi, K.; Inoue, M.; Takano, M.; Kageyama, H. *Nat. Mater.* **2012**, *11*, 507.

(30) Sancier, K. M.; Inami, S. H. *J. Catal.* **1968**, *11*, 135.

(31) Sermon, P. A.; Bond, G. C. *Catal. Rev.: Sci. Eng.* **1974**, *8*, 211.

(32) Prins, R. *Chem. Rev.* **2012**, *112*, 2714.

(33) Khoobiar, S. *J. Phys. Chem.* **1964**, *68*, 411.

(34) Sancier, K. M. *J. Catal.* **1971**, *23*, 298.

(35) Dickens, P. G.; Hibble, S. J.; Jarman, R. H. *J. Electron. Mater.* **1981**, *10*, 999.

DOI: 10.1021/jacs.6b05396
J. Am. Chem. Soc. 2016, 138, 9316−9324

(36) Vasilopoulou, M.; Douvas, A. M.; Georgiadou, D. G.; Palilis, L. C.; Kennou, S.; Sygellou, L.; Soultati, A.; Kostis, I.; Papadimitropoulos, G.; Davazoglou, D.; Argitis, P. *J. Am. Chem. Soc.* **2012**, *134*, 16178.
(37) Fleisch, T. H.; Mains, G. J. *J. Chem. Phys.* **1982**, *76*, 780.
(38) Zhou, Y.; Ma, J.; Hu, E.; Yu, X.; Gu, L.; Nam, K.; Chen, L.; Wang, Z.; Yang, X. *Nat. Commun.* **2014**, *5*, 5381.
(39) Bellessa, J.; Symonds, C.; Vynck, K.; Lemaitre, A.; Brioude, A.; Beaur, L.; Plenet, J. C.; Viste, P.; Felbacq, D.; Cambril, E.; Valvin, P. *Phys. Rev. B: Condens. Matter Mater. Phys.* **2009**, *80*, 033303.
(40) Wang, F.; Li, Q.; Lin, L.; Peng, H.; Liu, Z.; Xu, D. *J. Am. Chem. Soc.* **2015**, *137*, 12006.
(41) Sha, X. W.; Chen, L.; Cooper, A. C.; Pez, G. P.; Cheng, H. S. *J. Phys. Chem. C* **2009**, *113*, 11399.
(42) Goodenough, J. B. *Prog. Solid State Chem.* **1971**, *5*, 145.
(43) Ingham, B.; Hendy, S. C.; Chong, S. V.; Tallon, J. L. *Phys. Rev. B: Condens. Matter Mater. Phys.* **2005**, *72*, 075109.
(44) Greenblatt, M. *Chem. Rev.* **1988**, *88*, 31.
(45) Tinet, D.; Legay, M. H.; Gatineau, L.; Fripiat, J. J. *J. Phys. Chem.* **1986**, *90*, 948.
(46) Schrinner, M.; Ballauff, M.; Talmon, Y.; Kauffmann, Y.; Thun, J.; Moller, M.; Breu, J. *Science* **2009**, *323*, 617.
(47) He, R.; Wang, Y.; Wang, X.; Wang, Z.; Liu, G.; Zhou, W.; Wen, L.; Li, Q.; Wang, X.; Chen, X.; Zeng, J.; Hou, J. *Nat. Commun.* **2014**, *5*, 4327.
(48) Qian, X.; Kuwahara, Y.; Mori, K.; Yamashita, H. *Chem. - Eur. J.* **2014**, *20*, 15746.
(49) Ma, X.; Dai, Y.; Yu, L.; Huang, B. *Light: Sci. Appl.* **2016**, *5*, e16017.
(50) Kresse, G.; Furthmuller, J. *Phys. Rev. B: Condens. Matter Mater. Phys.* **1996**, *54*, 11169.
(51) Blochl, P. E. *Phys. Rev. B: Condens. Matter Mater. Phys.* **1994**, *50*, 17953.
(52) Perdew, J. P.; Burke, K.; Ernzerhof, M. *Phys. Rev. Lett.* **1996**, *77*, 3865.
(53) Kresse, G.; Joubert, D. *Phys. Rev. B: Condens. Matter Mater. Phys.* **1999**, *59*, 1758.

DOI: 10.1021/jacs.6b05396
J. Am. Chem. Soc. 2016, 138, 9316−9324